ORIGINAL PAPER

Dynamic response and chaotic behavior of a controllable flexible robot

Caixia Ban[ID] · **Ganwei Cai**[ID] · **Wei Wei**[ID] ·
Sixu Peng

Abstract Flexible robots with controllable mechanisms have advantages over common tandem robots in vibration magnitude, residual vibration time, working speed, and efficiency. However, abnormal vibration can sometimes occur, affecting their operation. Traditionally only simple mechanisms are considered in studying abnormal vibration, omitting reference to important chaotic phenomena caused by the flexibility of the mechanism rod. In order to better understand the causes of abnormal vibration, our work takes a controllable flexible robot with a complex series-parallel mechanism as a research object and uses a combination of Lagrangian and finite element methods to establish its nonlinear elastic dynamics. The effectiveness of the model is verified by comparing the calculated frequency with the frequency measured in a test. The time-domain diagram, phase diagram, Poincaré map, maximum Lyapunov exponent, and bifurcation diagram of the elastic motion of the robot wrist are studied, and the chaotic phenomena in the system are identified through the phase diagram, Poincaré map, the maximum Lyapunov exponent, and the bifurcation diagram. The relationship between the parameters of the robot motion and the maximum Lyapunov exponent is discussed, including trajectory angular speed and radius. The results show that chaotic behavior exists in the controllable flexible robot and that trajectory angular speed and radius all have an influence on the chaotic motion. Our work provides a theoretical basis for further research on the control and optimal design of flexible robot mechanisms.

Keywords Controllable mechanism · Robots · Dynamic behavior · Chaos

G. Cai · W. Wei · S. Peng
College of Mechanical Engineering, Guangxi University, Nanning 530004, China
e-mail: caiganwei@163.com

C.Ban
College of Civil Engineering and Architecture, Guangxi University, Nanning 530004, China
e-mail: ban_caixia@163.com

G. Cai (✉)
School of Construction Machinery, Hunan Sany Polytechnic College, Changsha 410129, China

1 Introduction

Controllable mechanisms include adjustable mechanisms, hybrid drive mechanisms, variable input parameter mechanisms, and flexible robots. Controllable flexible robots have the following advantages over traditional robots: higher intelligence, greater flexibility of output motion, and higher accuracy of motion. They belong to a class of highly coupled nonlinear systems with complex nonlinear dynamic behaviors. Chaos is one of the most important dynamic characteristics of a nonlinear dynamic system. It is a bounded irregular motion distinct from periodic motion and quasi-periodic motion. It can well describe the behavior of nonlinear systems. The elastic deformation of mecha-

nism rods can cause the mechanism to behave chaotically. At present, the methods of analyzing chaotic motion of a system include the time history method, the phase diagram method, the Poincaré mapping method, the maximum Lyapunov exponent method, and the bifurcation diagram method [1–4], etc. It is therefore important to study the dynamic response and the chaotic behavior of controllable flexible robots, and establish the dynamic performance design theory of this type of robot, which will help establishing further characteristics of the nonlinear dynamic behavior of this system and in revealing its abnormalities [5–8].

In the past few decades, many researchers have worked on the dynamic response of robots. Tang et al. [9], based on Hamilton's principle, established a set of nonlinear equations of motion of a double-cable single-link flexible manipulator with two boundary constraints and studied the natural frequency and terminal response of the system. The effectiveness of the cable in suppressing the vibration of the system was verified by both simulation and experiment. Cai et al. [10] proposed a multi-objective optimization design method to improve the elastic strain response distribution of a joint strain gauge in the working area, and conducted related experimental studies to improve the sensitivity and resolution of the joint torque sensor, finally achieving compliance control of the robot joints. Amer et al. [11–15] used a Lagrangian method to establish nonlinear dynamic models of single-pendulum, double-pendulum, and triple-pendulum systems. A multi-scale method was used to solve the problem analytically. The solvability condition was checked and the time history and resonance response of the solution were obtained. Using a nonlinear stability analysis method, the stable and unstable regions were analyzed, and the influences of different physical parameters on dynamic motion were investigated. These models and their study have been important advances in the understanding of vibration control of construction machinery. Li et al. [16] studied the kinematic accuracy and dynamic performance of spatially deployable mechanisms taking into account the uncertainties of geometric and physical parameters, including the uncertainty of joint clearance. They used the Monte Carlo method to solve the dynamic equation. My et al. [17] proposed a general two-link flexible robot dynamic modeling method, carried out inverse dynamic response analysis, and verified the effectiveness and robustness of the method through numerical calculation. Sun et al. [18] estab-

lished a simplified dynamic model of a flexible manipulator with interval gaps and random material characteristics. Their numerical-analysis results showed that joint clearance, component flexibility, and uncertainty all have a strong influence on the kinematic accuracy and dynamic behavior of the flexible manipulator. Meng et al. [19] established a dynamic model of a planar single-link flexible manipulator by using the hypothetical mode method and proposed a fast and stable control strategy based on the system energy to achieve suppression of the flexible rod's vibration. He et al. [20–23] used the hypothetical mode method, concentrated spring-mass model method, and other methods, including neural network control methods, for flexible link manipulators, to achieve trajectory tracking and vibration suppression. Zhou et al. [24] used space-vector theory and graph theory to study the dynamic coupling effects of multi-arm space robots, focusing on the effects of dynamic parameters, link lengths, and joint variables on coupling. Cuvillon et al. [25] used the theory of modal analysis to derive a dynamic model of the modal space, which is useful for adjusting the damping modal controller; this analysis was verified by experiments on an eight-cable suspension robot prototype.

Researchers have also done considerable work on the chaotic analysis of mechanisms considering the flexibility link, joint clearance, and time-varying stiffness. Chen et al. [26–28] established an ideal nonlinear relative dynamics model of the 4-UPS-UPU flexible parallel mechanism and the two-degrees-of-freedom 9-bar mechanism and studied the dynamic response, phase diagram, and Poincaré map of the mechanisms. The mapping and the largest Lyapunov exponent verified the existence of chaos in the complex mechanical system. Cao et al. [29] introduced the fractional-order model of a magnetically coupled broadband energy harvester under low-frequency excitation, using phase trajectories, power spectra, Poincaré maps, and bifurcation diagrams to analyze fractional-order damping, excitation amplitude, and frequency pairs. Lampart et al. [30] discussed the dynamic characteristics of a non-autonomous double pendulum model under soft-stop dual-harmonic excitation, and performed simulations for a specific range of excitation frequencies, confirming that many bifurcations change the characteristics of induced motion into regular, quasi-periodic, and chaotic motions. Jiang et al. [31] studied a cracked gear system in a coal cutter considering the environmental multi-frequency excitation force, and analyzed the

amplitude-frequency relationship of the model's main resonance using the multi-scale method; they also calculated the dynamic response of the model by the incremental harmonic balance method. Qi et al. [32] proposed a spherical chaotic system based on appropriately combining a conservative system with a dissipative system under the celestial mechanism and studied the rich dynamics of four types of spherical system: having spherical four-wing chaotic attractors, spherical ring-like chaotic attractors, spherical periodic orbits, and spherical sink orbits. Based on previous theoretical studies, Moysis et al. [33] proposed an improved HyperJerk system, with a hyperbolic sine function as the only nonlinear term, and studied the path to chaos, antimonotonicity, crisis and coexistence attractors, etc. Miranda-Colorado et al. [34] proposed a hybrid speed controller for flexible joint robots, which can induce chaotic motion on the manipulators of such robots with multiple degrees of freedom. Based on Lyapunov theory, the asymptotic stability of the tracking error signal is verified when the controller is used.

This paper reports our work analyzing the dynamic response and chaotic behavior of a controllable flexible robot. Using the finite element method and Lagrangian equations, an elastodynamic model of the robot is proposed. We establish the law of motion of the robot's end trajectory, compare the natural frequency of the system by using a numerical method and the hammer test method to verify the reliability of the nonlinear dynamic model. The nonlinear dynamic response of the system is analyzed, including the time-domain diagram, the phase diagram, the Poincaré map, the maximum Lyapunov exponent, and the bifurcation diagram. The chaotic state of the system is identified. Finally, the relationship between the motion parameters of the system and the maximum Lyapunov exponent is analyzed, including the radius and angular velocity of the circular trajectory. This lays a foundation for further analysis of the nonlinear characteristics of the system.

2 Kinematic analysis of the controllable flexible robot

The vibration of an industrial robot will reduce its efficiency, shorten its working life, and reduce its accuracy, so it is of great importance to suppress the robot's vibration. The controllable robot applies the "multi-degrees-of-freedom controllable mechanism" theory to
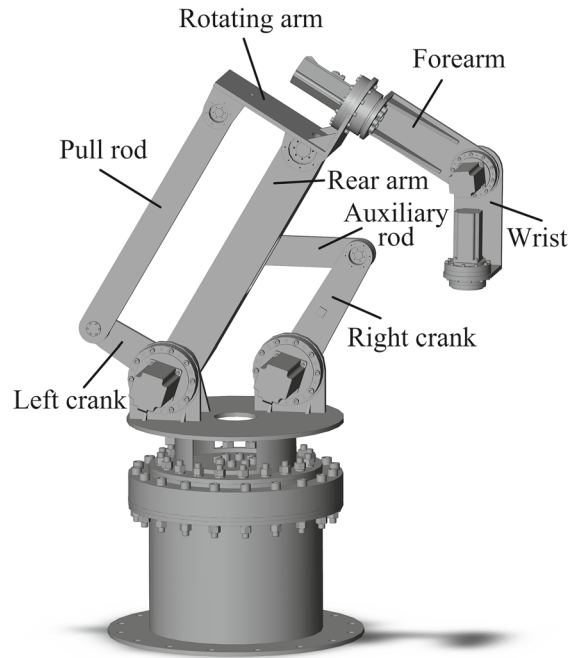

Fig. 1 Three-dimensional model of a controllable flexible robot

the field of robot mechanics. This approach installs the drive motor and reducer on the frame as much as possible and increases the local closed-chain mechanism, thereby reducing the joint's large moment of inertia. The prototype structure consists mainly of a waist, left crank, pull rod, rotating arm, rear arm, auxiliary rod, right crank, forearm, and wrist. The design of the prototype can improve the load capacity and working accuracy while satisfying the requirements of light weight, fast movement, high reliability, and high stability. Figure 1 shows a three-dimensional model of a controllable flexible robot, and Fig. 2 shows a schematic diagram of such a robot.

In kinematic analysis, in order to study the movement of the wrist, one can overlook the rods that make up two parallelograms, and simplify the movement into a classic tandem mechanism, considering only the waist, rear arms, rotating arms, forearms, and wrists. The corresponding joints are all revolving joints, and the angular displacement is used as the relative displacement to meet the requirement that the operation adapts to a complex trajectory. For each joint, the z-axis is in the direction of right-handed rotation, the x-axis is usually in the direction of the common perpendicular to the two z-axis, and the y-axis is always
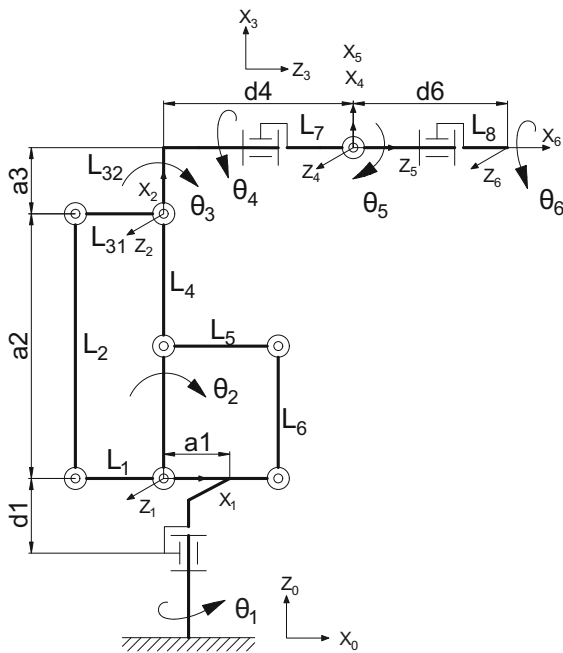
Fig. 2 Schematic diagram of a controllable flexible robot

perpendicular to both the x-axis and z-axis, as shown in Fig. 2. A corresponding local coordinate system is established at each joint. The rotation axis of joint i is z_{i-1}, the first coordinate system (coordinate system 0) coincides with the global coordinate system, and the i-th link is located between joints $i - 1$ and i, in turn analogy. The kinematic relationship between adjacent members of the manipulator can be described by the Denavit–Hartenberg (D–H) [35] model, for which the transformation matrix is

$$A_i^{i-1} = Rot(z, \theta_i) Tran(0, 0, d_i) Tran(a_i, 0, 0) Rot(x, \alpha_i)$$

$$= \begin{bmatrix} cos(\theta_i) & -cos(\alpha_i)sin(\theta_i) & sin(\alpha_i)sin(\theta_i) & a_i cos(\theta_i) \\ sin(\theta_i) & cos(\alpha_i)cos(\theta_i) & -sin(\alpha_i)cos(\theta_i) & a_i sin(\theta_i) \\ 0 & sin(\alpha_i) & cos(\alpha_i) & d_i \\ 0 & 0 & 0 & 1 \end{bmatrix}$$

(1)

where $\theta_i \in R^n (i = 1, 2, ..., 6)$ is the generalized coordinate of the joint of the manipulator, d_i is the offset of the connecting rod, a_i is the length of the connecting rod, and α_i is the torsion angle of the connecting rod.

The total transformation from the robot-wrist coordinate system to the global coordinate system is

$$^0T_6 = A_1^0 A_2^1 A_3^2 A_4^3 A_5^4 A_6^5 \tag{2}$$

Given the angle of the joint θ_i, the position and posture of the wrist can be determined by using Eq. (2).

The first 3×3 columns of the matrix $^0T_6$ are the postures of the wrist, and the fourth column represents the position of the wrist. It can be written in the following unified form:

$$p = f(\theta) \tag{3}$$

where p is the position of the wrist.

By differentiating Eq. (3), the relationship between the moving velocity $\dot{p}$ of the wrist and the angular velocity $d\theta/dt$ of the joint can be calculated.

$$\frac{dp}{dt} = J \frac{d\theta}{dt} \tag{4}$$

where

$$J = \frac{\partial f(\theta)}{\partial \theta^T} = \begin{bmatrix} \frac{\partial f_1}{\partial \theta_1} & \cdots & \frac{\partial f_1}{\partial \theta_n} \\ \vdots & \ddots & \vdots \\ \frac{\partial f_m}{\partial \theta_1} & \cdots & \frac{\partial f_m}{\partial \theta_n} \end{bmatrix} \tag{5}$$

For a definite motion $\varphi(p)$, in order to meet the requirements of high-precision control of robot motion, a closed-loop synchronous control scheme is introduced, which includes, for the joint's angular velocity and angular acceleration,

$$\begin{aligned} \dot{\theta} &= J^{-1}\dot{p} \\ \ddot{\theta} &= J^{-1}(\ddot{p} - \dot{J}\dot{\theta}_s + k_v e_2 + k_p e_1) \end{aligned} \tag{6}$$

where k_v and k_p are negative definite matrices; e_1 and e_2 are the rigid displacement error and velocity error of the wrist, respectively, and $\dot{\theta}_s$ is the initial joint angular velocity.

3 Elastodynamic model of the controllable flexible robot

Given that modern machinery is developing rapidly in the direction of higher speed, greater precision, and lighter weight, the influence of component deformation on the stability and operating accuracy of the robot cannot be ignored. In order to make the controllable flexible robot achieve better dynamic performance, it is necessary to carry out an elastodynamic analysis. Based on the Lagrangian equation and finite element method, an elastodynamic model of the controllable flexible robot can be established. To simplify the modeling, we make the following assumptions:

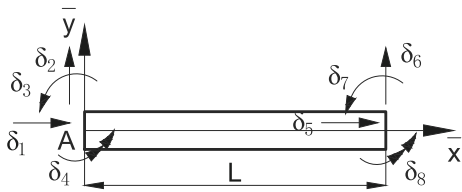(1) The waist is treated as a rigid member, the other members as elastic.

Fig. 3 Beam element and element generalized coordinate

(2) According to the kinematic assumption, by ignoring the coupling of rigid-body motion and elastic deformation, the real motion can be regarded as a linear superposition of the two.

(3) Using the assumption of instantaneous structure at a certain mechanism position, the rotating coordinate system is treated as a static coordinate system, the rotation angle is treated as a constant, and the rotation matrix is treated as a constant matrix.

(4) The mass of the bearing mounted at the hinge is treated as a concentrated mass, which is superimposed onto the system mass matrix, ignoring the influence of clearance and friction.

3.1 Model of beam element

Figure 3 shows a typical beam-element structure diagram. The element coordinate system $A\overline{x}\,\overline{y}$, which is fixed to the beam element, is established in the diagram. The transverse displacement and longitudinal displacement of the beam element are functions not only of the element coordinate $\overline{x}$, but also of time t. It is assumed that the transverse displacement and longitudinal displacement of any point are expressed by $w(\overline{x}, t)$ and $u(\overline{x}, t)$, respectively. The transverse displacement function uses a fifth-order polynomial, and the longitudinal displacement uses a first-order polynomial:

$$\begin{cases} u(\overline{x}, t) = N_{iA}^T \delta_i \\ w(\overline{x}, t) = N_{iB}^T \delta_i \end{cases} \quad (7)$$

In these equations, δ_i is the unit generalized coordinate, and the generalized coordinate array is $\delta_i = [\delta_1, \delta_1, \cdots, \delta_8]^T$. N_{iA}, N_{iB} are the displacement functions, which depend on the unit coordinate $\overline{x}$.

$$\begin{aligned} N_{iA} &= \begin{bmatrix} 1 - e\ 0\ 0\ 0\ e\ 0\ 0\ 0 \end{bmatrix}^T \\ N_{iB} &= \begin{bmatrix} 0\ u_1\ u_2\ u_3\ 0\ u_4\ u_5\ u_6 \end{bmatrix}^T \end{aligned} \quad (8)$$

and

$$u_1 = 1 - 10e^3 + 15e^4 - 6e^5$$

$$\begin{aligned} u_2 &= L(e - 6e^3 + 8e^4 - 3e^5) \\ u_3 &= \frac{1}{2}L^2(e^2 - 3e^3 + 3e^4 - e^5) \\ u_4 &= 10e^3 - 15e^4 + 6e^5 \\ u_5 &= L(-4e^3 + 7e^4 - 3e^5) \\ u_6 &= \frac{1}{2}L^2(e^3 - 2e^4 + e^5) \end{aligned}$$

Here $e = \overline{x}/L$; it is called the relative coordinate of the beam element, where L is the length of the element.

3.2 Dynamic model of beam element

3.2.1 Kinetic energy of beam element

Assuming that the cross section of the beam element is a uniform rectangle and that the mass of the section is concentrated on the axis, and ignoring the rotational kinetic energy of the section, the kinetic energy T of the beam element can be written

$$T = \frac{1}{2} \int_0^L \rho A \left[\left(\frac{du_a(\overline{x}, t)}{dt} \right)^2 + \left(\frac{dw_a(\overline{x}, t)}{dt} \right)^2 \right] d\overline{x} \quad (9)$$

where A is the cross-sectional area of the beam element and ρ is the density of the beam.

According to the simplified model assumption (2), it can be concluded that

$$\begin{cases} u_a(\overline{x}, t) = u_r(\overline{x}, t) + u(\overline{x}, t) \\ w_a(\overline{x}, t) = w_r(\overline{x}, t) + w(\overline{x}, t) \end{cases} \quad (10)$$

where $u_r(\overline{x}, t)$ and $w_r(\overline{x}, t)$ are the rigid-body displacements of points along the x and y axes, respectively.

Bringing the real movement of the mechanism into Eq. (9), the kinetic energy of the beam element can be expressed as

$$T = \frac{1}{2}(\dot{\delta}_r + \dot{\delta})^T m_e (\dot{\delta}_r + \dot{\delta}) \quad (11)$$

where m_e is the element quality matrix,

$$m_e = \rho A \int_0^L N N^T d\overline{x} \quad (12)$$

3.2.2 Deformation energy of beam element

When deriving the deformation energy, only the bending deformation of the beam under the action of the

Table 1 Structural parameters of the controllable flexible robot

i-th link	θ	d	a	α	Joint	Range
1	θ_1	0.1	−0.15	$\pi/2$	Rotation	(−160, 160)
2	θ_2	0	0.6	0	Rotation	(20, 120)
3	θ_3	0	0.1725	$\pi/2$	Rotation	(−70, 70)
4	θ_4	0.366	0	$-\pi/2$	Rotation	(−170, 170)
5	θ_5	0	0	$\pi/2$	Rotation	(−90, 90)
6	θ_6	0.257	0	0	Rotation	(−180, 180)

bending moment and the tensile and compressive deformation caused by the action of the axial force are taken into account. Other kinds of deformation, such as shear, are ignored. According to the mechanics of materials, the deformation energy can be written

$$V = \frac{1}{2} \int_0^L EA \left(\frac{\partial u(\overline{x}, t)}{\partial \overline{x}} \right)^2 d\overline{x}$$
$$+ \frac{1}{2} \int_0^L EI \left(\frac{\partial^2 w(\overline{x}, t)}{\partial \overline{x}^2} \right)^2 d\overline{x} \tag{13}$$

where E is the elastic modulus of the beam element and I is the moment of inertia of the cross section of the beam element.

By substituting and simplifying Eq. (13), we get

$$V = \frac{1}{2} \delta^T k_e \delta \tag{14}$$

where k_e is the element stiffness matrix.

$$k_e = EA \int_0^L \dot{N}_A \dot{N}_A^T d\overline{x} + EI \int_0^L \ddot{N}_B \ddot{N}_B^T d\overline{x} \tag{15}$$

3.2.3 Differential equation of beam element

Incorporating Eqs. (11) and (14) above into the second type of Lagrangian equation, one gets

$$\frac{d}{dt} \left(\frac{\partial T}{\partial \dot{\delta}} \right) - \frac{\partial T}{\partial \delta} + \frac{\partial V}{\partial \delta} = \overline{f} \tag{16}$$

The dynamic equation of the beam element in a rotating coordinate system is

$$\overline{m} \ddot{\delta}_i + \overline{k} \delta_i = f_i + p_i - \overline{m} \ddot{\delta}_{ir} \tag{17}$$

where $\overline{f}$ is the element generalized force array, including the external force array f_i and the force array between the units p_i, which will cancel each other in the process of mechanism assembly, and $\ddot{\delta}_r$ is the element rigid-body acceleration array.

In order to transform the assembly of the equation of motion of the elements into the equation of motion of the system, a new generalized coordinate array of elements is introduced:

$$\delta_{ie} = [\delta_{1e} \quad \delta_{2e} \quad \cdots \quad \delta_{8e}]^T \tag{18}$$

According to the assumption (3), the relationship between δ_i and δ_{ie} is

$$\delta_i = R_i \delta_{ie} \tag{19}$$

where R_i is the coordinate transformation matrix.

The differential equation of motion of the beam element in the global coordinate system is

$$m \ddot{\delta}_{ie} + k \delta_{ie} = f - m \ddot{\delta}_{ire} \tag{20}$$

where $m = R^T \overline{m} R$, $k = R^T \overline{k} R$, and $f = R^T \overline{f} R$ are all 8×8 symmetric matrices.

3.3 Differential equation of the controllable flexible robot

The left crank, right crank, and wrist are cantilever beams. The pull rod and rear arm are each divided into two units. The other members are all single units. A total of 11 units make up the controllable flexible robot system. The generalized coordinate array of the system is defined as

$$U = [U_1 \quad U_2 \quad \cdots \quad U_{N_u}]^T \tag{21}$$

where $N_u = 42$ is the total number of generalized coordinates.

The relationship between δ_{ie} and U is written

$$\delta_{ie} = B_i U \tag{22}$$

where B_i is the coordinate harmony matrix.

In the process of studying the actual working of the controllable mechanism robot, the influence of damping cannot be ignored. In this work, the elastodynamic

Table 2 Material characteristic parameters and moment of inertia of the controllable flexible robot

Component	Left crank	Pull rod	Rotating arm	Rear arm	Auxiliary rod	Right crank	Forearm	Wrist
Length [m]	L_1	L_2	L_{31}	L_4	L_5	L_6	L_7	L_8
	0.2	0.6	0.2	0.6	0.26	0.3	0.366	0.257
	L_{s1}	L_{s2}	L_{32}	L_{s4}	L_{s5}	L_{s6}	–	–
	0.1	0.3	0.1725	0.3	0.13	0.15	–	–
Mass [kg]	1.677	4.222	4.274	12.68	1.994	2.440	3.699	3.145
Moment of inertia [kg.m²]	8.40×10^{-3}	1.474×10^{-1}	3.026×10^{-2}	4.443×10^{-1}	1.681×10^{-2}	2.314×10^{-2}	7.633×10^{-3}	2.816×10^{-2}

equation is included, in the form of a Rayleigh damping matrix [36–39]. All of the unit dynamics equations are assembled to obtain the differential equations of motion of the system:

$$M\ddot{U} + C\dot{U} + KU = F - M\ddot{U}_r \tag{23}$$

where $\ddot{U}_r$ is the system rigid-body acceleration array. $M = \sum_{i=1}^{N_e} M_{ie}$, $C = \sum_{i=1}^{N_e} C_{ie}$, $K = \sum_{i=1}^{N_e} K_{ie}$, and $F = \sum_{i=1}^{N_e} F_{ie}$ are the system mass matrix, damping matrix, stiffness matrix, and generalized force array, respectively, and N_e is the total number of elements.

4 Dynamic response analysis of the controllable flexible robot

The elastodynamic equation of the system, Eq. (23), is a time-varying strongly coupled nonlinear differential equation. In our work, the direct-integration implicit Newmark method and the fourth-order Runge–Kutta algorithm are used to solve the dynamic response of the mechanism.

The structure parameters, material characteristic parameters, and moment of inertia of the controllable mechanism robot are shown in Tables 1 and 2 and Table 2. In analyzing the dynamic response of the controllable flexible robot, the period of the motion is defined as T, with $T = \frac{2\pi}{\omega}$. The integral step is $0.01s$. The initial position of the robot wrist is specified as

$$p = (x_0, y_0, z_0)^T = (0.5532, 0, 0.329 + R)^T$$

where R is the radius of the circular trajectory.

The controllable mechanism robot moves according to the circular trajectory described by the following equations:

$$\begin{cases} X = x_0 - R\sin(\omega t) \\ Y = y_0 \\ Z = z_0 - R\cos(\omega t) \end{cases} \tag{24}$$

Here, ω is the angular velocity of the circular trajectory.

Through numerical simulation, the characteristics of the natural frequency of the system are analyzed, and the time-history diagrams of the elastic displacement, velocity, and acceleration of the robot wrist in the x direction, the y direction, and around the z direction are obtained.

4.1 Analysis of frequency characteristics of the controllable flexible robot

The natural frequency of the mechanism is determined by the inherent characteristics of the mechanism (such as mass, shape, and material), and to changes in the position and attitude of the mechanism. By studying the natural frequency of the mechanism, we can grasp the vibration of the system as a whole, avoid a resonance phenomenon of the system, and benefit by the stability of the system. The average value of the natural frequency can express the overall change trend of the mechanism frequency in the entire motion cycle and is an important indicator for evaluating the dynamic characteristics of the mechanism. Among them, the first-order natural frequency (fundamental frequency) plays an important role in the dynamic response of the system, which is the focus in both engineering applications and theoretical research.

By using the classical multi-point excitation single-point pick-up modal test method in the force measurement modal test, 14 tested points are selected and marked on the rod mechanism of the controllable flexible robot, and a three-way accelerometer is installed at the end of the robot manipulator, serving as the pick-up point in the modal test. We tap each measuring point in turn, collect the force signal and acceleration signal at each measuring point, then calculate the fundamental frequency of the system. The experimental measurement system for the natural frequency of the controllable flexible robot is shown in Fig. 4, where the robot is stopped in the upright position for testing through the operating handle of the control system. The joint angular position is $\theta = [0\ \pi/2\ 0\ 0\ 0\ 0]^T$. The modal frequency of the system obtained by experiment is 6.836 Hz. The natural frequency, calculated by the numerical simulation method, is 6.84 Hz. The difference between the experimental value and the numerically calculated value is 0.11%, confirming that the elastodynamic model of the controllable flexible robot has high reliability.

Based on the circular motion trajectory given by the mechanism, MATLAB is used to program the numerical simulation. When $\omega = 0.5\pi$, the relationship between the radii of different circular trajectories and the first-order natural frequency of the system is analyzed, and when $R = 0.05$m, the relationship between the velocity of different circular trajectories and the first-order natural frequency of the system is analyzed.

It can be seen from Fig. 5 hat the first-order natural frequency of the system decreases as the radius of the circular track increases. With an increase of the angular velocity of the trajectory, the value of the first-order natural frequency also shows a downward trend, but the local curve fluctuates slightly. Since the natural frequency of each rod is affected by the movement of the mechanism, the overall natural frequency of the mechanism varies with its position.

4.2 Vibration response analysis of the controllable flexible robot

According to the law of motion of the circular trajectory of the system, the circular trajectory radius R of the controllable flexible robot is set to 0.05 m, the trajectory angular velocity ω is 0.5π rad/s, and the system material is ordinary carbon steel. The Newmark method is used to solve the nonlinear equations of the system, and the elastic displacement, velocity, acceleration, amplitude spectrum of the robot wrist are recorded.

Figures 6, 7, 8 show the elastic displacement, velocity, acceleration, and amplitude spectrum curves of the controllable flexible robot.

As the mechanism follows a circular trajectory, the elastic member of the system will be elastically deformed, causing errors in the vibration of the end manipulator arm, which in turn results in a decrease in the accuracy of the motion of the controllable flexible mechanism. It can be seen that the elastic movement displacement, speed, and acceleration of the mechanism in the x, y directions and around the z direction all have slight oscillations, with no obvious regularity. The frequency domain curves in all directions show the fundamental frequency of the system, which further illustrates the reliability of the elastodynamic modeling of the system.

5 Chaotic motion analysis of the controllable flexible robot

Although chaotic motion has long-term unpredictability, it does have unique mathematical characteristics that are very important for understanding regular aspects of chaos. In a phase plane diagram with velocity on the ordinate and displacement on the abscissa, one can make a trajectory that changes with time. If a closed

Fig. 4 Experimental measurement system of the natural frequency of the controllable flexible robot
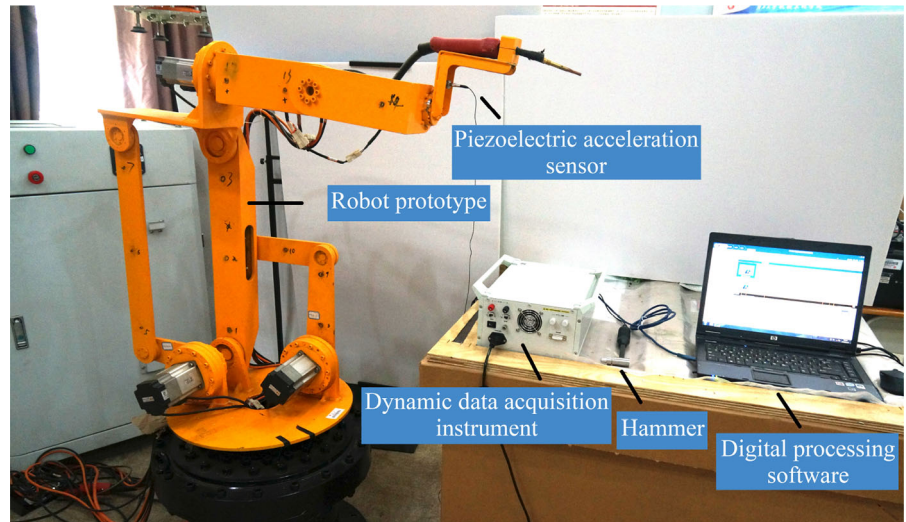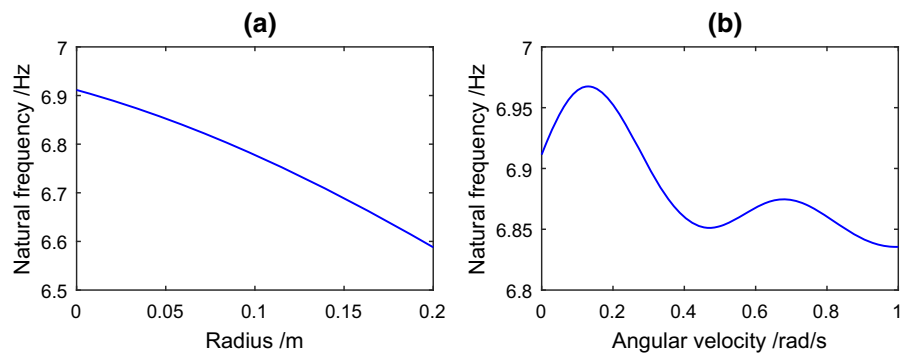

Fig. 5 The dependence of first-order natural frequency on (a) the radius of the circular trajectory and (b) the angular velocity of the circular trajectory

trajectory appears in the phase plane, the system has a periodic solution; otherwise, the system may produce chaotic motion. The phase diagram of the controllable flexible robot is shown in Fig. 9.

This figure depicts the phase trajectory diagram in the directions of x, y, z, and co-direction. It can be seen from the diagram that the phase trajectory is chaotic and disordered, with the trajectory remaining in the same region.

Through continuous mapping of the system, different forms of phase points or phase trajectories can be observed in the Poincaré map. According to its topological properties, it can be judged whether a system has period 1 motion, period k motion, quasi-periodic motion, or chaotic motion. The isolated points, finite (k) isolated points, closed curves, and uncountable point sets distributed in a certain area appearing on the Poincaré section can, respectively, represent the period 1 motion, period k motion, quasi-periodic motion, and

chaotic motion. The Poincaré section of the controllable flexible robot is shown in Fig. 10.

It can be seen from this figure that the Poincaré maps of the robot in the x and, y directions and around the z direction all consist of scattered and disorderly dense points, throughout the graphic area. Figures 9 and 10 both show that the controllable flexible robot system is in a state of chaos.

The Lyapunov exponent is a quantity that describes the degree of divergence of adjacent orbits in the phase space. In this work, the small data volume method [40] is used to estimate the maximum Lyapunov exponent. The concrete recipe for calculation is as follows:

(i) Perform FFT transformation on the time series $\{x(t_i), i = 1, 2, ..., N\}$.

(i) Calculate the time delay τ and the average period P, determine the embedding dimension m, and thereby reconstruct the phase space $\{Y_j, j = 1, 2, ..., M\}$.

Fig. 6 Time–frequency characteristics in the *x* direction. **a** Elastic displacement. **b** Amplitude spectrum. **c** Elastic velocity. **d** Elastic acceleration
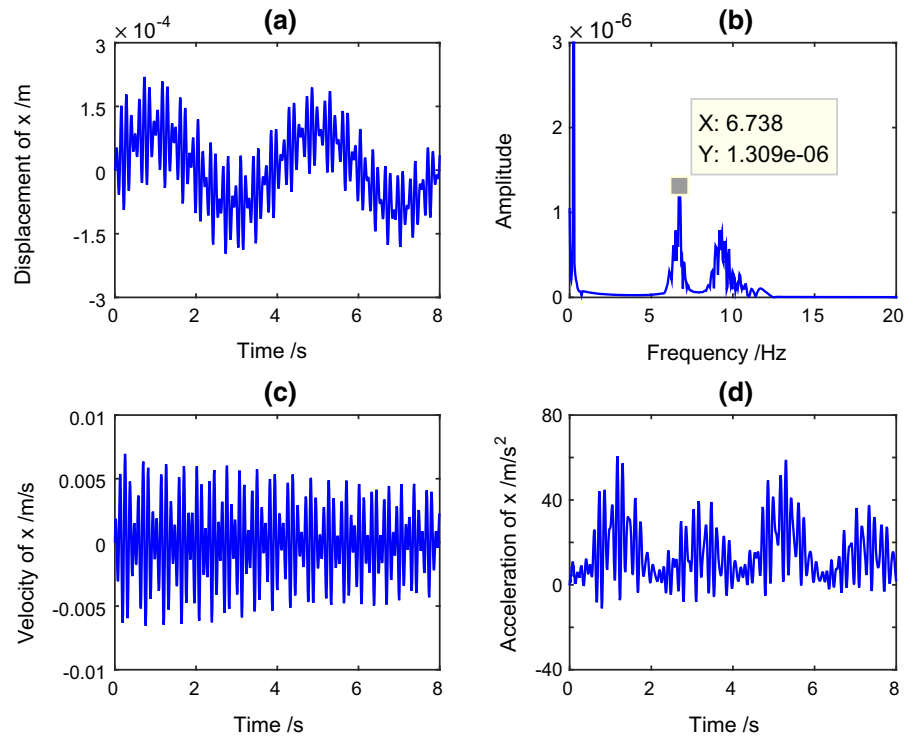

Fig. 7 Time–frequency characteristics in the *y* direction. **a** Elastic displacement. **b** Amplitude spectrum. **c** Elastic velocity. **d** Elastic acceleration
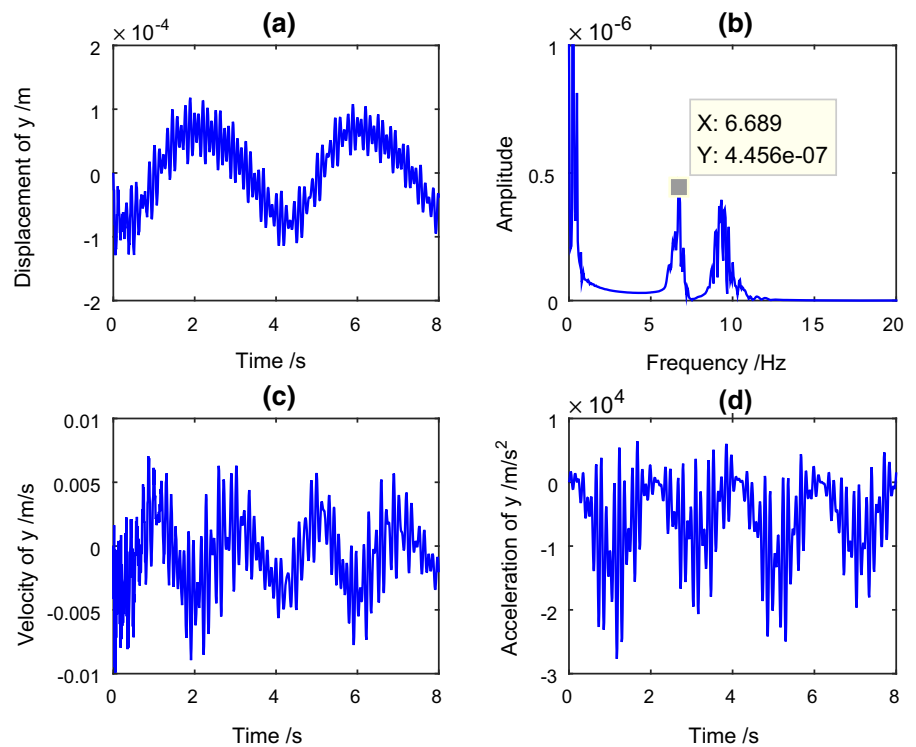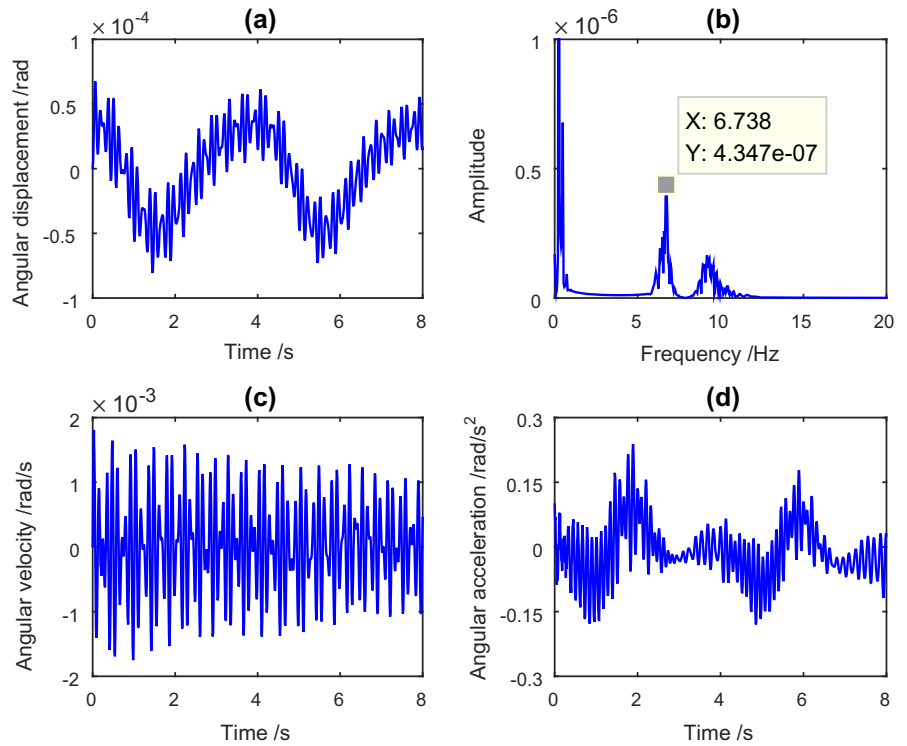
Fig. 8 Time–frequency characteristics around the *z* direction **a** Elastic displacement. **b** Amplitude spectrum. **c** Elastic velocity. **d** Elastic acceleration

Fig. 9 Phase diagram of mechanism. **a** Relative displacement and velocity in the *x* direction. **b** Relative displacement and velocity in the *y* direction. **c** Relative rotation angle and velocity around the *z* axis. **d** Relative displacement and velocity in the co-direction
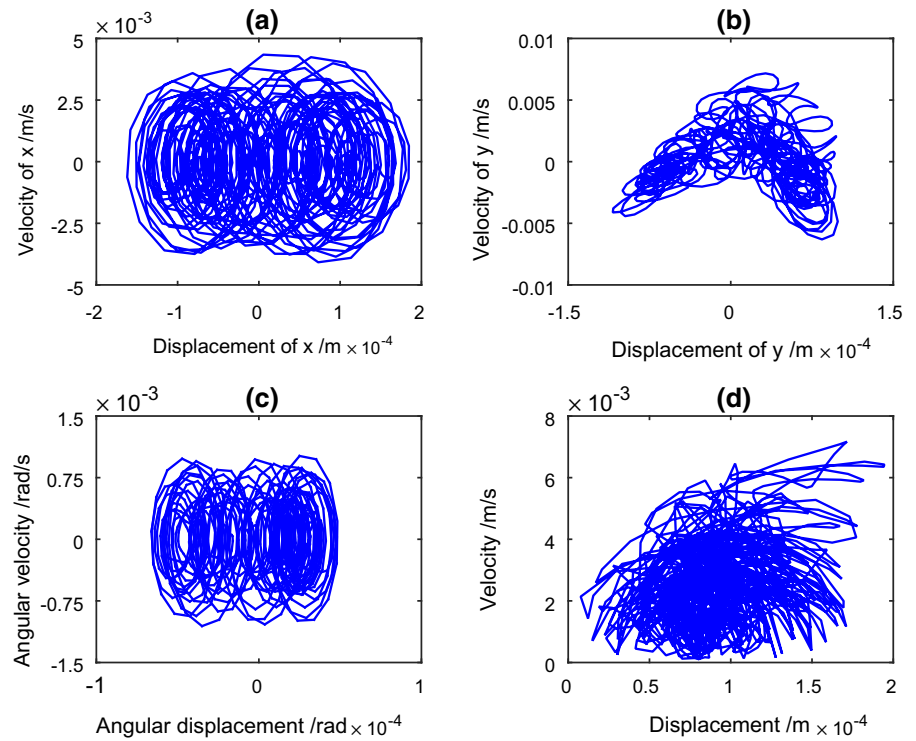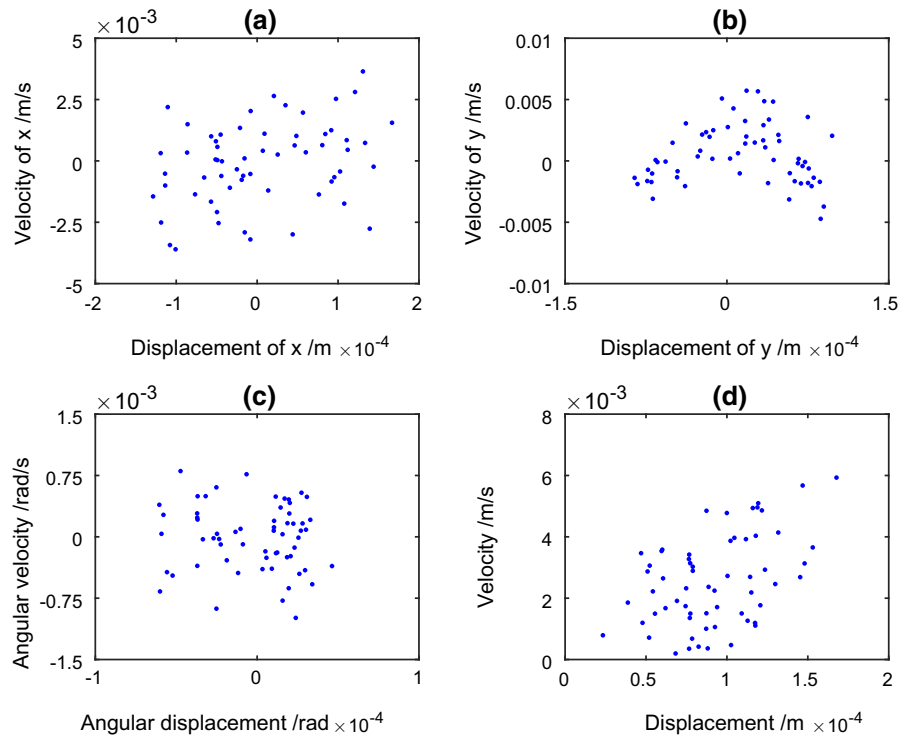
Fig. 10 Poincaré cross-sectional view of mechanism. **a** Relative displacement and velocity in the *x* direction. **b** Relative displacement and velocity in the *y* direction. **c** Relative rotation angle and velocity around the *z* axis. **d** Relative displacement and velocity in the co-direction

(iii) Calculate the nearest neighbor point Y_{j*} of each point Y_j in the phase space, and the distance between the two points, $d_j(0) = \min_{j*} \|Y_j - Y_{j*}\|, |j - j^*| > P$.

(iv) For each point Y_j in the phase space, calculate the distance $d_j(i)$, $d_j(i) = |Y_{j+i}, Y_{j*+i}|, i = 1, 2, ..., \min(M - j, m - j^*)$ after i discrete time steps of the adjacent point pair.

(v) Finally, find the average value of $\ln d_j(i)$ of all j for each i, that is, $y(i) = (\frac{1}{q \triangle t}) \sum_{j=1}^{q} \ln d_j(i)$, where q is the number of nonzero values of $d_j(i)$; and use the least squares method to draw a regression line, the slope of which is the maximum Lyapunov exponent.

When the Lyapunov exponent is negative, the mapping converges finally to a certain point; when it is zero, the mapping moves periodically; when it is positive, the mapping is in a chaotic state. The Lyapunov exponent of the controllable flexible robot in the directions of *x*, *y*, *z* and in combination is shown in Fig. 11.

As shown in this figure, the largest Lyapunov exponents are 0.4036 in the *x* direction, 0.1910 in the *y* direction, 0.1755 around the *z* direction, and 0.3058 in the combined direction. The fact that the maximum Lyapunov exponent of the system is greater than zero in all directions confirms that the controllable flexible robot is in a chaotic state.

Figure 12 depicts bifurcation diagrams for excitation frequency of the robot in the *x* direction, the *y* direction, around the *z* axis, and in the co-direction. According to this figure, when the external excitation changes from 0 to 0.16 Hz, the motion state of the wrist in all directions changes from periodic motion to chaotic motion. This shows that there is indeed chaos in the elastodynamic response of the controllable flexible robot.

6 Influence of the main motion parameters on the chaotic characteristics of the system

6.1 The influence of the radius of the circular trajectory on the chaotic motion of the system

In order to study the influence of the circular trajectory radius *R* on the chaotic motion of the system, the relationship between this radius and the maximum Lyapunov exponent of movement in each direction is established, as shown in Fig. 13.

Fig. 11 Lyapunov exponent graphs of all directions: **a** the *x* direction, **b** the *y* direction, **c** around the *z* axis, and **d** the co-direction
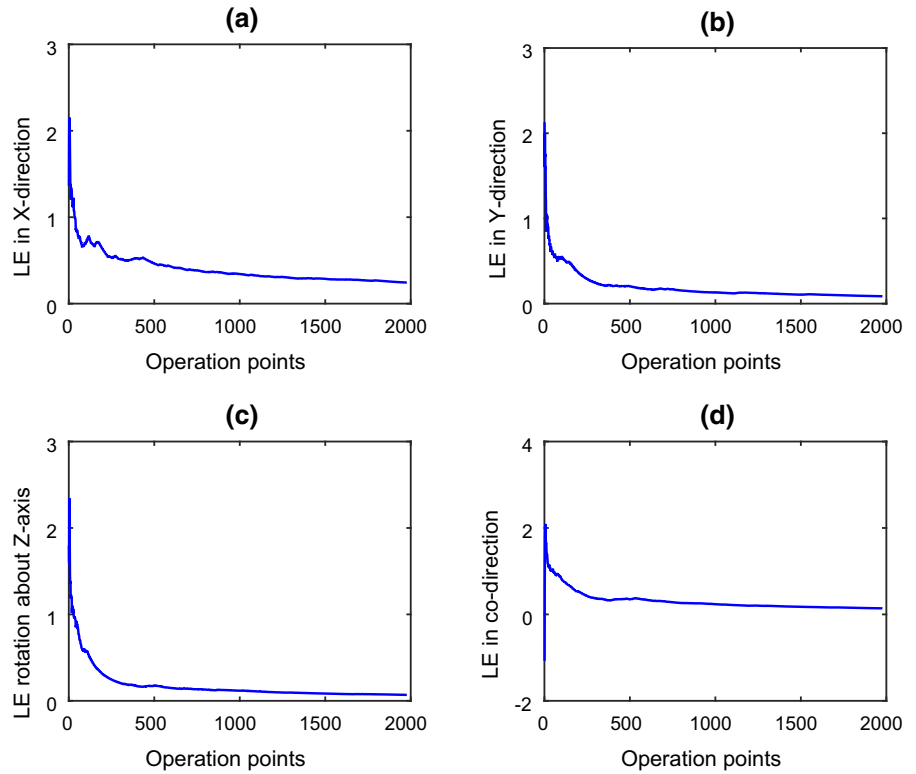

Fig. 12 Bifurcation diagrams with respect to excitation frequency of all directions: **a** the *x* direction, **b** the *y* direction, **c** around the *z* axis, and **d** the co-direction
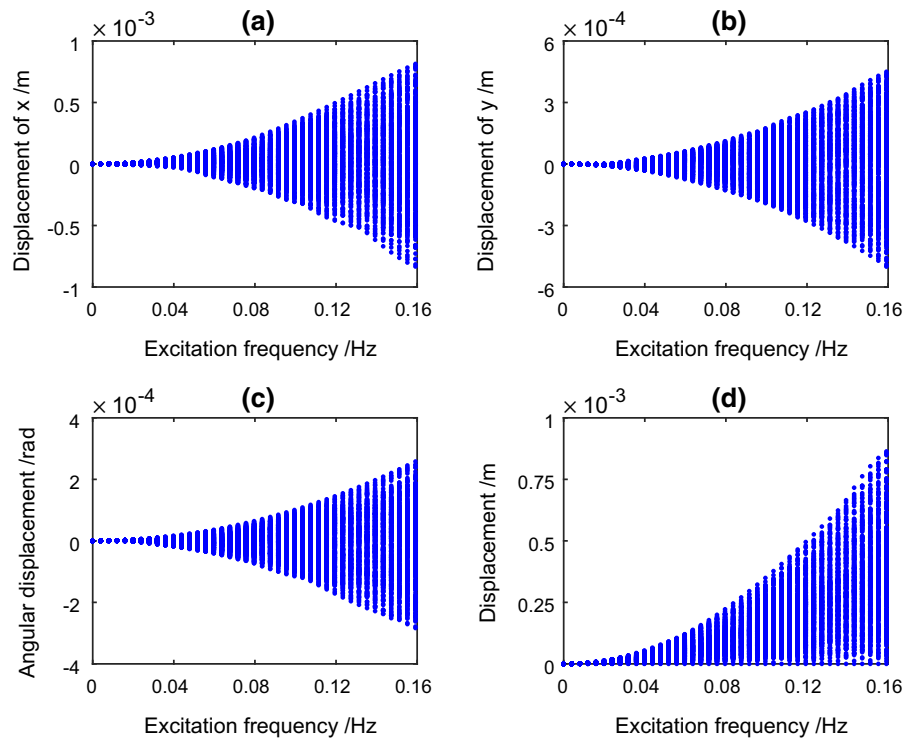
Fig. 13 The relationship between the maximum Lyapunov exponent and the radius of the circular trajectory **a** in the *x* direction, **b** in the *y* direction, **c** around the *z* axis, and **d** In the co-direction
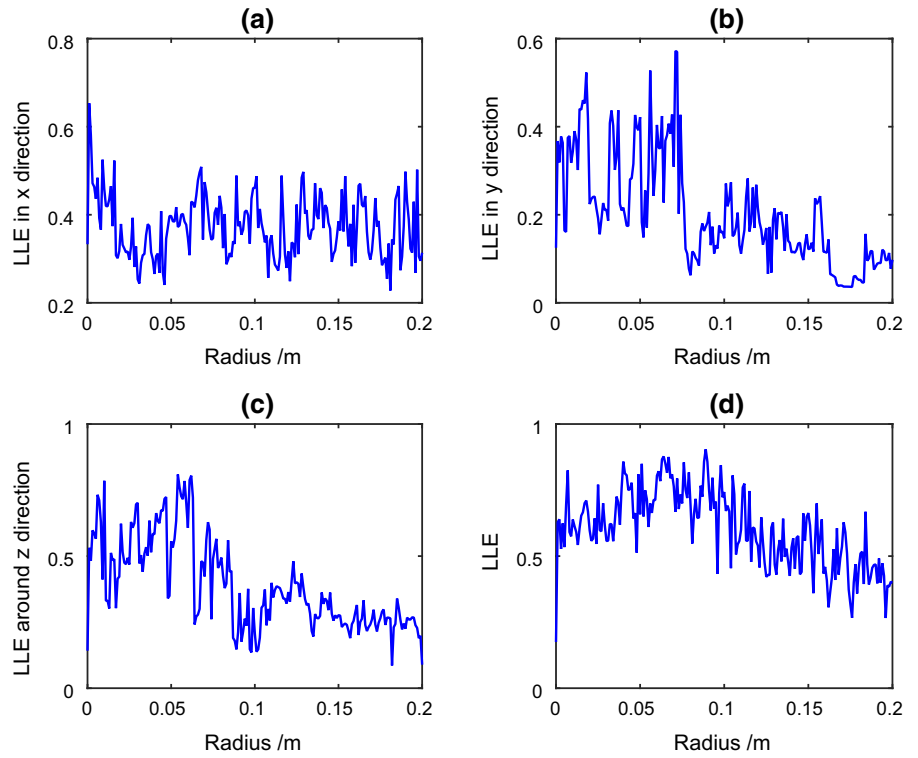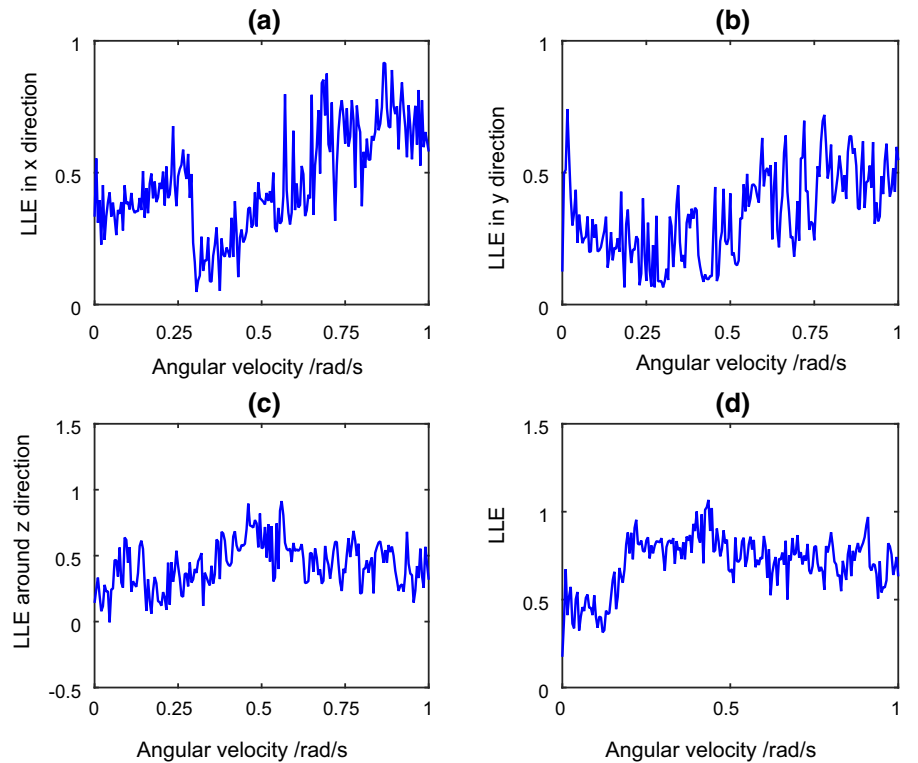

Fig. 14 The relationship between the maximum Lyapunov exponent and the velocity of the circular trajectory, **a** in the *x* direction, **b** in the *y* direction, **c** around the *z* axis, and **d** in the co-direction

As can be seen from this figure, with an increase of the radius R of the circular trajectory, the maximum Lyapunov exponents in the y direction and around the z direction show a downward trend, the maximum Lyapunov exponent in the x direction oscillates around 0.4, while the maximum Lyapunov exponent in the codirection increases at first and then decreases.

6.2 The influence of the angular velocity of the circular trajectory on the chaotic motion of the system

In order to study the influence of the angular velocity of the circular trajectory on the chaotic motion of the system, the relationship between the angular velocity of the circular trajectory and the maximum Lyapunov exponent of the movement in each direction was established, as shown in Fig. 14.

It can be seen in this figure that with an increase of the angular velocity ω of the circular trajectory, the maximum Lyapunov exponents in the x and y directions show an overall upward trend. When the angular velocity ω of the circular trajectory is 1 rad/s, the maximum Lyapunov exponent in the combined direction is the largest, 0.6323.

7 Conclusion

This paper establishes a nonlinear elastic dynamic model of a controllable flexible robot, obtains the nonlinear dynamic response characteristics of this new type of robot system, identifies the chaotic phenomenon in the system, and reveals the reason for the system's abnormal vibration. The main conclusions are the following: (I) Based on the Lagrange equation and the finite element method, the elastodynamic model of the controllable flexible robot system was established. The natural frequency of the robot was tested by a hammering test, and the validity of the nonlinear dynamic model was verified by comparing it with the numerical simulation results. (II) The elastic displacement, velocity, and acceleration of the wrist in accordance with the circular trajectory were analyzed. The simulation results show that the motion of the system has no obvious regularity. By analyzing the system phase diagram, Poincaré map, Lyapunov exponent, and bifurcation diagram, it was further verified that there is chaos in the elastic vibration of the controllable flexible robot under

the excitation of inertial force. (III) On this basis, the relationship between the changes in the main motion parameters and the maximum Lyapunov exponent was analyzed comprehensively and systematically. It was revealed that the radius of the trajectory and its angular velocity both have some influence on the nonlinear motion of the controllable flexible robot system. In future work, vibration suppression and joint clearance in controllable flexible robotic systems may be investigated, and this work will also be extended to 3D models.

Data availability The datasets generated during and/or analyzed during the current study are available from the corresponding author on reasonable request.

Declarations

Conflict of interest The authors declare that they have no conflict of interest.

References

1. Chegini, M., Sadati, H., Salarieh, H.: Chaos analysis in attitude dynamics of a flexible satellite. Nonlinear Dyn. **93**(3), 1421–1438 (2018)
2. Chegini, M., Sadati, H.: Chaos analysis in attitude dynamics of a satellite with two flexible panels. Int. J. Non Linear Mech. **103**, 55–67 (2018)
3. Toz, M.: Chaos-based Vortex Search algorithm for solving inverse kinematics problem of serial robot manipulators with offset wrist. Appl. Soft. Comput. **89**, 106074 (2020)
4. Singh, J.P., Koley, J., Lochan, K., Roy, B.K.: Presence of megastability and infinitely many equilibria in a periodically and quasi-periodically excited single-link manipulator. Int. J. Bifurc. Chaos **31**(2), 2130005 (2021)
5. Lochan, K., Roy, B.K., Subudhi, B.: A review on two-link flexible manipulators. Annu. Rev. Control **42**, 346–367 (2016)
6. Kvrgic, V., Vidakovic, J.: Efficient method for robot forward dynamics computation. Mech. Mach. Theory **145**, 103680 (2020)
7. Zhang, S., Wang, S., Jing, F., Tan, M.: Parameter estimation survey for multi-joint robot dynamic calibration case study. Sci. China Inf. Sci. **62**(10), 202203 (2019)

8. Wei, J., Cao, D., Liu, L., Huang, W.: Global mode method for dynamic modeling of a flexible-link flexible-joint manipulator with tip mass. Appl. Math. Model. **48**, 787–805 (2017)

9. Tang, L., Gouttefarde, M., Sun, H., Yin, L., Zhou, C.: Dynamic modelling and vibration suppression of a single-link flexible manipulator with two cables. Mech. Mach. Theory **162**, 104347 (2021)

10. Fu, B., Cai, G.: Design and calibration of a joint torque sensor for robot compliance control. IEEE Sens. J. **21**(19), 21378–21389 (2021)

11. Amer, W.S., Amer, T.S., Hassan, S.S.: Modeling and stability analysis for the vibrating motion of three degrees-of-freedom dynamical system near resonance. Appl. Sci. Basel **11**(24), 11943 (2021)

12. Amer, T., Bek, M., Hassan, S.: The dynamical analysis for the motion of a harmonically two degrees of freedom damped spring pendulum in an elliptic trajectory. Alex. Eng. J. **61**(2), 1715–1733 (2022)

13. Amer, T.S., Starosta, R., Elameer, A.S., Bek, M.A.: Analyzing the stability for the motion of an unstretched double pendulum near resonance. Appl. Sci. Basel **11**(20), 9520 (2021)

14. Abady, I., Amer, T., Gad, H., Bek, M.: The asymptotic analysis and stability of 3DOF non-linear damped rigid body pendulum near resonance. Ain Shams Eng. J. **13**(2), 101554 101554 (2022)

15. Amer, T.S., Galal, A.A., Abolila, A.F.: On the motion of a triple pendulum system under the influence of excitation force and torque. Kuwait J. Sci. **48**(4), 1–17 (2021)

16. Li, J., Huang, H., Yan, S., Yang, Y.: Kinematic accuracy and dynamic performance of a simple planar space deployable mechanism with joint clearance considering parameter uncertainty. Acta Astronaut. **136**, 34–45 (2017)

17. My, C.A., Bien, D.X.: New development of the dynamic modeling and the inverse dynamic analysis for flexible robot. Int. J. Adv. Robot. Syst. **17**(4), 1–12 (2020)

18. Sun, D., Zhang, B., Liang, X., Shi, Y., Suo, B.: Dynamic analysis of a simplified flexible manipulator with interval joint clearances and random material properties. Nonlinear Dyn. **98**(2), 1049–1063 (2019)

19. Meng, Q.X., Lai, X.Z., Wang, Y.W., Wu, M.: A fast stable control strategy based on system energy for a planar single-link flexible manipulator. Nonlinear Dyn. **94**(1), 615–626 (2018)

20. He, W., David, A.O., Yin, Z., Sun, C.: Neural network control of a robotic manipulator with input deadzone and output constraint. IEEE Trans. Syst. Man Cybern. Syst. **46**(6), 759–770 (2016)

21. Sun, C., He, W., Hong, J.: Neural network control of a flexible robotic manipulator using the lumped spring-mass model. IEEE Trans. Syst. Man Cybern. Syst. **47**(8), 1863–1874 (2017)

22. Gao, H., He, W., Zhou, C., Sun, C.: Neural network control of a two-link flexible robotic manipulator using assumed mode method. IEEE Trans. Ind. Inform. **15**(2), 755–765 (2019)

23. He, W., Ouyang, Y., Hong, J.: Vibration control of a flexible robotic manipulator in the presence of input deadzone. IEEE Trans. Ind. Inform. **13**(1), 48–59 (2017)

24. Zhou, Y., Luo, J., Wang, M.: Dynamic coupling analysis of multi-arm space robot. Acta Astronaut. **160**, 583–593 (2019)

25. Cuvillon, L., Weber, X., Gangloff, J.: Modal control for active vibration damping of cable-driven parallel robots. J. Mech. Robot. **12**(5), 051004 (2020)

26. Chen, X., Li, Y., Deng, Y., Li, W., Wu, H.: Kinetoelastodynamics modeling and analysis of spatial parallel mechanism. Shock Vib. **2015**, 938314 (2015)

27. Chen, X., Wu, L., Deng, Y., Wang, Q.: Dynamic response analysis and chaos identification of 4-UPS-UPU flexible spatial parallel mechanism. Nonlinear Dyn. **87**(4), 2311–2324 (2017)

28. Chen, X., Jiang, S., Deng, Y., Wang, Q.: Dynamics analysis of 2-DOF complex planar mechanical system with joint clearance and flexible links. Nonlinear Dyn. **93**(3), 1009–1034 (2018)

29. Cao, J., Zhou, S., Inman, D.J., Chen, Y.: Chaos in the fractionally damped broadband piezoelectric energy generator. Nonlinear Dyn. **80**(4), 1705–1719 (2015)

30. Lampart, M., Zapomel, J.: Dynamics of a non-autonomous double pendulum model forced by biharmonic excitation with soft stops. Nonlinear Dyn. **99**(3), 1909–1921 (2020)

31. Jiang, Y., Zhu, H., Li, Z., Peng, Z.: The nonlinear dynamics response of cracked gear system in a coal cutter taking environmental multi-frequency excitation forces into consideration. Nonlinear Dyn. **84**(1), 203–222 (2016)

32. Qi, G., Chen, G.: A spherical chaotic system. Nonlinear Dyn. **81**(3), 1381–1392 (2015)

33. Moysis, L., Petavratzis, E., Marwan, M., Volos, C., Nistazakis, H., Ahmad, S.: Analysis, synchronization, and robotic application of a modified hyperjerk chaotic system. Complexity **2020**, 2826850 (2020)

34. Miranda-Colorado, R., Aguilar, L.T., Moreno-Valenzuela, J.: A model-based velocity controller for chaotization of flexible joint robot manipulators: Synthesis, analysis, and experimental evaluations. Int. J. Adv. Robot. Syst. **15**(5), 1–15 (2018)

35. Denavit, J., Hartenberg, R.: A kinematic notation for lower-pair mechanisms based on matrices. J. Appl. Mech. Trans. ASME **22**, 215–221 (1995)

36. Danguang, P., Genda, C., Zuocai, W.: Suboptimal Rayleigh damping coefficients in seismic analysis of viscously-damped structures. Earthq. Eng. Eng. Vib. **13**(4), 653–670 (2014)

37. Cruz, C., Miranda, E.: Evaluation of the Rayleigh damping model for buildings. Eng. Struct. **138**, 324–336 (2017)

38. Onitsuka, S., Ushio, Y., Ojima, N., Iijima, T.: Modeling method of element Rayleigh damping for the seismic analysis of a 3D FEM model with multiple damping properties. J. Vib. Control **24**(17), 4065–4077 (2018)

39. Salehi, M., Sideris, P.: Enhanced Rayleigh damping model for dynamic analysis of inelastic structures. J. Struct. Eng. **146**(10), 04020216 (2020)

40. Rosenstein, M.T., Collins, J.J., Luca, C.: A practical method for calculating largest lyapunov exponents from small data sets. Phys. D Nonlinear Phenom. **65**(1–2), 117–134 (1993)